



# Black phosphorus-CdS-La<sub>2</sub>Ti<sub>2</sub>O<sub>7</sub> ternary composite: Effective noble metal-free photocatalyst for full solar spectrum activated H<sub>2</sub> production

Liang Mao<sup>a,b</sup>, Xiaoyan Cai<sup>a,b</sup>, Songqiu Yang<sup>c</sup>, Keli Han<sup>c</sup>, Junying Zhang<sup>b,\*</sup>

<sup>a</sup> School of Materials Science and Engineering, China University of Mining and Technology, Xuzhou 221116, PR China

<sup>b</sup> Key Laboratory of Micro-nano Measurement, Manipulation and Physics (Ministry of Education), Department of Physics, Beihang University, Beijing 100191, PR China

<sup>c</sup> State Key Laboratory of Molecular Reaction Dynamics, Dalian Institute of Chemical Physics, Chinese Academy of Sciences, Dalian 116023, PR China

## ARTICLE INFO

### Keywords:

Black phosphorus  
Noble metal-free  
Near-Infrared light  
Photocatalytic hydrogen production  
Charge transfer dynamics

## ABSTRACT

Wide-bandgap semiconductor photocatalysts such as La<sub>2</sub>Ti<sub>2</sub>O<sub>7</sub> (LTO) are stable but can only work under ultraviolet (UV) light, while narrow-bandgap semiconductor photocatalysts such as CdS and black phosphorus (BP) with broad-wavelength range absorption generally have low stability and high electron-hole pairs recombination rate. In this work, ternary heterostructure composing of BP quantum dots (QDs), CdS nanoparticles (NPs) and LTO nanosteps (NSP) is developed for the first time to make full use of their respective advantages, which offers a promising approach to achieving desired stability and solar energy harvesting. As an effective noble metal-free photocatalyst, BP-CdS-LTO composite generates H<sub>2</sub> from Na<sub>2</sub>S/Na<sub>2</sub>SO<sub>3</sub> aqueous solution with a rate of 0.96 mmol g<sup>-1</sup> h<sup>-1</sup> under solar light irradiation, and 0.26 mmol g<sup>-1</sup> h<sup>-1</sup> in the near-infrared (NIR) range. In this system, BP serves as a NIR photosensitizer; CdS not only contributes to visible light absorption but also bonds with BP to promote the transmission of photogenerated charge carriers; LTO absorbs UV light as well as provides reaction sites for photoinduced electrons. Femtosecond transient absorption spectroscopy is used to elucidate the kinetics of the injection of photogenerated electrons from BP QDs to CdS NPs and finally to LTO. This work provides deep insight into charge transfer between semiconductors with different band alignments, which can open a new avenue for more rationally designing heterostructured photocatalysts for H<sub>2</sub> production.

## 1. Introduction

To meet the sustainable development needs of the world, hydrogen (H<sub>2</sub>) evolved from photocatalytic water splitting, as a promising technique to provide clean solar fuels, has been developed in recent decades [1,2]. So far, diverse semiconductor photocatalysts such as oxides, sulfides, oxynitrides have been employed for photocatalytic splitting of water [3–5]. Unfortunately, there is no single semiconductor that can meet all the requirements of effective photocatalyst. The semiconductors with wide band gap are stable but have a limited spectral absorption range [6]. For instance, high-stable perovskite structured La<sub>2</sub>Ti<sub>2</sub>O<sub>7</sub> (LTO) exhibits good photocatalytic activity toward water splitting, but its wide band gap (*ca.* 3.2 eV) limits its light absorption within the ultraviolet (UV) region [7,8]. On the contrary, many semiconductors with relatively narrow band gap can absorb wider range of solar spectrum but suffer from photocorrosion during photocatalysis [9]. For instance, CdS with band gap of approximately 2.3 eV matches well with the visible spectral range of the sunlight, but the photocatalytic performance is usually restricted by its low photostability and

high recombination rate of photoinduced electron-hole pairs [10,11]. Moreover, only a few narrow bandgap semiconductors can absorb near-infrared (NIR) light, which accounts for more than 40% of the solar energy, and most of them usually bear either low photocatalytic efficiency based on narrow absorption or synthetic difficulty [12,13]. For instance, black phosphorus (BP) has been drawing increasing attention in recent years because of its anisotropic two-dimensional (2D) layered structure with tunable band gap in the range of 0.3–2.0 eV and the earth-abundance [14–17]; however, the utilization of BP for NIR light driven photocatalytic H<sub>2</sub> evolution has been rarely reported, and its photocatalytic activity is still very low because of the rapid charge recombination [18,19].

Alternatively, combining wide-bandgap and narrow-bandgap semiconductors to form binary or ternary heterostructures makes full use of their respective advantages, which provides an effective approach to allowing efficient solar energy harvesting [20]. For example, Majima's group has developed a BP-Au/LTO composite to harvest visible to NIR light for water splitting [21]. By absorbing this broad sweep of energy, BP nanosheets (NSs) were stimulated to release electrons, which were

\* Corresponding author.

E-mail address: [zjy@buaa.edu.cn](mailto:zjy@buaa.edu.cn) (J. Zhang).

<https://doi.org/10.1016/j.apcatb.2018.10.007>

Received 2 September 2018; Received in revised form 27 September 2018; Accepted 5 October 2018

Available online 08 October 2018

0926-3373/ © 2018 Elsevier B.V. All rights reserved.

then conducted to Au nanoparticles (NPs) coating on the LTO NSs. Although a breakthrough on above ternary heterostructure was achieved, two key points still need to be considered. Firstly, the low-positioned conduction band (CB) edge endows BP NSs a poor water reduction activity, leading to the thermodynamic electron injection difficulty from BP NSs to other wide band gap semiconductors. Although the addition of Au NPs realized the electron delivery from BP to LTO NSs in the above funding, an up-conversion process happened since Au NPs had to absorb an extra photon in order to endow the electrons with high enough potential to transfer into LTO NSs. Secondly, noble metal was used in this work, like many other researches. The high-cost and limited reserves of noble metals trigger the exploring of alternative noble metal-free photocatalysts.

In the present work, a noble metal-free photocatalyst system composing of BP quantum dots (QDs), CdS NPs and LTO nanosteps (NSP) was developed for the first time to generate  $H_2$  under a broad-wavelength range solar light irradiation, especially in the NIR region. Herein, BP QDs function as UV to NIR photosensitizer, which possess improved water reduction activity compared with the common BP nanosheets [22]; CdS NPs not only contribute to UV–vis light harvesting but also serve as electron relay that facilitate charge transfer between the BP QDs and LTO; Nanostep structured LTO has been demonstrated to separate electron and hole spatially by successive surface heterojunction, exhibiting higher electron flow and remarkably long-lived charges [23,24]. The electron injection dynamics from photoexcited BP QDs to CdS NPs and then to LTO is fully investigated by using femtosecond transient absorption spectroscopy. This work opens up a new approach to taking advantage of the excellent charge transport property of the wide-bandgap semiconductor and the broad spectral absorption of narrow-bandgap semiconductor, while simultaneously promoting the overall photostability and efficient interfacial charge transfer from the QDs to the metal sulphide and oxide without any noble metal assistance.

## 2. Experimental section

### 2.1. Materials

Bulk BP was purchased from Nanjing XFNANO Materials Tech Co., China (XF161, purity > 99.998%). N-methyl-2-pyrrolidone (NMP,  $\geq 98.0\%$ ), lanthanum oxide ( $La_2O_3$ ,  $\geq 97.0\%$ ), potassium chloride (KCl,  $\geq 99.0\%$ ), cadmium sulfate ( $CdSO_4$ ,  $\geq 98.0\%$ ), thiourea ( $CH_4N_2S$ ,  $\geq 99.7\%$ ), sodium sulphide ( $Na_2S \cdot 9H_2O$ ,  $\geq 98.0\%$ ), sodium sulfite ( $Na_2SO_3$ ,  $> 97.0\%$ ), ammonium hydroxide ( $NH_3 \cdot H_2O$ , 28 wt% in water), and ethyl alcohol ( $C_2H_5OH$ ,  $\geq 99.7\%$ ) were purchased from Beijing Chemical Industry, China. All chemicals were used without further purification. Deionized water ( $H_2O$ , 99.99%) was purchased from Beijing Longfen Co., China.

### 2.2. Preparation of BP quantum dots

The BP QDs were prepared using a modified liquid exfoliation method involving ultrasound probe sonication followed by ice-bath sonication of ball-milled bulk BP powders, as described in our previous publication [22].

### 2.3. Preparation of CdS-LTO composites

LTO nanosteps were synthesized by molten-salt method, following our previous publications [23,24]. CdS NPs were *in situ* deposited on the surface of LTO using a chemical bath deposition. Briefly, 1 M ammonia solution, 1 mM  $CdSO_4$  and 5 mM thiourea were firstly dissolved. The LTO NSP was then dispersed in the CdS precursor solution under a water bath of 60 °C. After stirring for 10 min, the CdS deposited LTO nanostructures were washed with deionized water and then annealed in a  $N_2$  flow at 400 °C for 2 h. Bare CdS nanoparticles were prepared under

the same condition without the addition of LTO NSP.

### 2.4. Preparation of BP-CdS-LTO composites

BP-CdS-LTO ternary hybrids were obtained through a self-assembly process. 50 mg of CdS-LTO was ultrasonically dispersed in 100 mL deionized water to form a homogeneous dispersion. Afterwards, certain volume of BP QDs aqueous solution was introduced. The mixtures were kept stirring overnight. The powders were collected by high-speed centrifugation, and then dried in vacuum at 40 °C overnight, resulting in BP-CdS-LTO composites.

### 2.5. Characterizations

The samples were characterized using X-ray diffraction (XRD) (Bruker D/max-V2500, Germany) with a Cu target and  $K\alpha$  radiation ( $\lambda = 1.54056 \text{ \AA}$ ), scanning electron microscopy (SEM) (Zeiss microscope, Germany), transmission electron microscopy (TEM) (JEM-2100 F instrument, Japan) at an acceleration voltage of 200 kV, and X-ray photoelectron spectroscopy (XPS) (ESCALAB 250Xi instrument, Thermo Fisher Scientific, USA). The Raman spectra were recorded on an Andor 500i spectrograph with a 532 nm laser. The UV-vis-NIR absorption and diffuse reflectance spectra were measured by using Shimadzu UV-3600 spectrophotometer (Japan) at room temperature.

### 2.6. Photocatalytic $H_2$ production

20 mg of photocatalyst was dispersed in 40 mL of aqueous solution containing  $Na_2S$  (0.35 M) and  $Na_2SO_3$  (0.25 M) in a 100 mL quartz reactor connected with an automatic sampling equipment (SUNCAT Instruments PGS-15, China). Prior to the irradiation, the reactor was sealed and then vacuumed to completely remove the gas. The sample was irradiated using a Xe lamp (Beijing Bofeilai Co., China; 300 mW  $cm^{-2}$ ) with constant stirring and kept at room temperature through a recirculating cooling water system. The volume of the generated  $H_2$  was automatically measured through a gas chromatograph (Jingkeruida SP6900, China). The apparent quantum efficiency (AQE) was calculated as  $AQE = (2 \times \text{number of evolved } H_2 \text{ molecules} / \text{number of incident photons}) \times 100\%$ .

### 2.7. Photoelectrochemical measurements

Photoelectrochemical (PEC) measurements were conducted in three-electrode quartz cells connected with a 660E electrochemical analyzer (Shanghai Chenhua, China). Platinum wire and Ag/AgCl electrode were employed as the counter electrode, and reference electrode, respectively. LTO, CdS and BP film on glassy carbon electrode (Shanghai Sanse, China) served as the working electrode.  $Na_2SO_4$  aqueous solution (0.1 M) was used as the electrolyte. Mott-Schottky (M–S) curves were measured under an ac amplitude of 10 mV and frequency of 1 kHz. The photocurrents and electrochemical impedance spectroscopy (EIS) plots were obtained under a bias of 1.23 V vs. reversible hydrogen electrode (RHE).

### 2.8. Transient absorption measurements

A pump-probe laser system based on a regenerative amplified Ti:sapphire laser system from Coherent (800 nm, 35 fs, and 1 kHz repetition rate) was used for the femtosecond Transient absorption (TA) measurements. By using a 460 or 620 nm laser pulse generated by a TOPAS optical parametric amplifier (OPA) which was pumped by the 800 nm pulse, the samples were excited. The power of the pump beam in front of the sample was kept at 0.2  $\mu J/cm^2$ . The probe beam was a white light continuum (WLC) generated by a 2 mm thick sapphire window from 430 to 750 nm. A motorized delay stage was used to control the delay between the pump and probe pulses. The TA spectra

were measured by using a quartz cuvette with a path length of 1 mm at room temperature.

## 2.9. Computational details

We performed the calculations by using the density functional theory (DFT) within the generalized-gradient approximation (GGA) with the exchange-correlation functional of Perdew-Burke-Ernzerhof (PBE). This has been implemented in the Vienna Ab Initio Simulation Package (VASP), which spans reciprocal space with a plane-wave basis and uses the projector-augmented wave (PAW) method [25,26]. For the plane-wave basis set, a cutoff of  $E_{\text{cut}} = 500$  eV and a  $3 \times 1 \times 1$  Monkhorst-Pack k-point mesh have been used for the energy calculations. During the relaxations, only atoms of the CdS (110) slab structures are allowed to relax with an energy convergence of  $10^{-4}$  eV and forced convergence of 0.03 eV/Å. In the case of slabs, the vacuum space is 15 Å.

## 3. Results and discussion

### 3.1. Morphology, structure and optical property

The phase identification and composition analysis of the as-prepared samples were performed from XRD and Raman spectra. Shown in Fig. 1a are the XRD patterns of the pristine LTO, LTO loaded with 3 wt% CdS (CdS-LTO), and CdS-LTO loaded with 1 wt% BP (BP-CdS-LTO). All XRD peaks of the pristine LTO can be indexed to the monoclinic phase  $\text{La}_2\text{Ti}_2\text{O}_7$  with a perovskite structure belonging to the P21 space group (JCPDS No. 70-0903). For CdS-LTO and BP-CdS-LTO samples, in addition to  $\text{La}_2\text{Ti}_2\text{O}_7$  diffraction peaks, CdS peak at  $32.8^\circ$  can be clearly observed. However, no signals assignable to BP are detectable in the ternary composites, plausibly as a result that BP is ultrasmall and is uniformly distributed on the CdS-LTO, as demonstrated in the EDS and TEM images below. To prove the existence of BP in BP-CdS-LTO, Raman spectra were performed, as shown in Fig. 1b. The characteristic peaks of LTO, CdS and BP components constitute the Raman spectra of BP-CdS-LTO. Noticeably, both BP QDs and BP-CdS-LTO exhibit three prominent peaks at  $361\text{ cm}^{-1}$ ,  $436\text{ cm}^{-1}$  and  $463\text{ cm}^{-1}$ , which can be assigned to the well-documented out-of-plane phonon modes ( $A_{1g}$ ) of BP, and two in-plane modes, that is,  $B_{2g}$  and  $A_{2g}$  of BP, respectively [27].

Fig. S1a shows a typical SEM image of pristine LTO, and it can be clearly seen that the LTO particles exhibit three-dimensional (3D) step-like surface topography with about 200–500 nm length and 70–100 nm width. With regard to CdS-LTO composites, one can see that CdS loading does not change the step structure of LTO. The size of the deposited CdS nanoparticles becomes larger as the CdS content increases from 1 to 7 wt% (Fig. S1b–e). Fig. S1f displays the BP QDs loaded CdS-LTO ternary composites, with the similar morphology of CdS-LTO. The corresponding EDX elemental mapping in Fig. S2 demonstrates the hybridization of BP and CdS-LTO. Weight ratio of P, Cd, S, La, Ti and O are obtained through EDX analysis of the selected area of Fig. S2a, indicating that the BP-CdS-LTO sample contains about 1 wt% of BP and

3 wt% of CdS (Fig. S3).

TEM images in Fig. 2a and b show ultrasmall BP QDs with lateral size of 3–5 nm resulted from liquid exfoliation method. From high resolution TEM (HRTEM) image in Fig. 2b inset, two sets of crystal lattice fringes of 0.18 and 0.17 nm with an intersection angle of  $76.4^\circ$  are observed, corresponding to (112) and (200) facet of orthorhombic phase black phosphorus, respectively. Fig. 2c is the TEM image of LTO nanostep, where the uniform strip-like structures on the surface of LTO particle are the edge/boundary of steps. Corresponding HRTEM and Fast Fourier Transform (FFT) pattern in Fig. 2d evidence the single-crystalline nature of the whole nanostep. After an *in-situ* growth process, CdS particles with about 6 nm sizes are uniformly coated on the step-structured LTO surfaces. The crystal lattice fringes of 0.31 nm detected on the nanoparticles are attributed to CdS (111) facet (Fig. 2f). The morphology of BP-CdS-LTO ternary composite loaded with 3 wt% of CdS and 1 wt% of BP (Fig. 2g) is very similar to that of CdS-LTO (Fig. 2e), while HRTEM image in Fig. 2h clearly shows the different lattice fringes of 0.30, 0.31, and 0.26 nm, corresponding to LTO, CdS, and BP, respectively. The HAADF-STEM image of this piece of BP-CdS-LTO hybrid and corresponding EDX elemental mapping evidently indicate the homogeneous distribution of BP and CdS on LTO (Fig. S4).

The surface chemical compositions and bonding states of the materials were analyzed by XPS. As compared with La 3d and Ti 2p spectra (Fig. 3a and b) of LTO, a slight shift of all La 3d and Ti 2p peaks to higher binding energy can be noticed in those of CdS-LTO. This phenomenon can be explained by an interaction of LTO and CdS, originating from the *in-situ* growth of CdS on LTO [28]. Comparing BP-CdS-LTO with CdS-LTO, it is found that there is no change in La 3d and Ti 2p signals after BP loading, implying the low interaction between LTO and BP. In Fig. 3c, LTO-CdS exhibits symmetric Cd 3d<sub>5/2</sub> and Cd 3d<sub>3/2</sub> peak at 405.1 and 411.8 eV, respectively, with a peak separation of 6.7 eV, being in good agreement with the energy splitting reported for CdS [29]. Binding energy of Cd 3d in BP-CdS-LTO exhibits slight increase relative to that of CdS-LTO, which may be ascribed to the decreased electron densities of Cd atoms due to the bonding between S and P as discussed below. In S 2p spectrum (Fig. 3d) of CdS-LTO, S 2p<sub>5/2</sub> peak at 161.7 eV and S 2p<sub>3/2</sub> peak at 162.8 eV correspond to Cd-S bonds in the CdS [30,31]. In contrast, S 2p in BP-CdS-LTO is broadened and is deconvoluted into four peaks. The additional peaks at 161.9 and 163.1 eV can be assigned to P-S bonds of BP and CdS [29,32]. The O 1s region (Fig. 3e) is fitted by two peaks in LTO, in which the Ti-O appears at 529.8 eV, and the physisorption of (OH) or chemisorbed H<sub>2</sub>O appears at 531.3 eV. Upon CdS modification, additional peak located at 532.0 eV appears, corresponding to S-O bonds. O 1s spectrum derived from BP-CdS-LTO is deconvoluted into four components, including Ti-O, H-O, S-O, and P-O bands. P-O bonds came from the slightly oxidized surface of BP QDs during and after exfoliation process [33,34]. To confirm the interaction of BP and CdS-LTO, P 2p spectra of pure BP QDs and BP-CdS-LTO are investigated. Fig. 3f shows three bands at ca. 128.7, 129.4, and 132.8 eV assigning to binding energies of P 2p<sub>3/2</sub>, P 2p<sub>1/2</sub>, and oxidized phosphorus (P=O), respectively [34]. In addition to these assigned peaks, a new peak at 133.8 eV appears in BP-CdS-LTO,

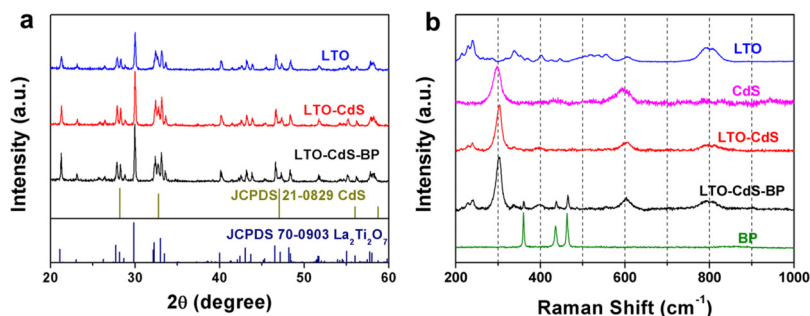


Fig. 1. XRD patterns (a) and Raman spectra (b) of different samples.



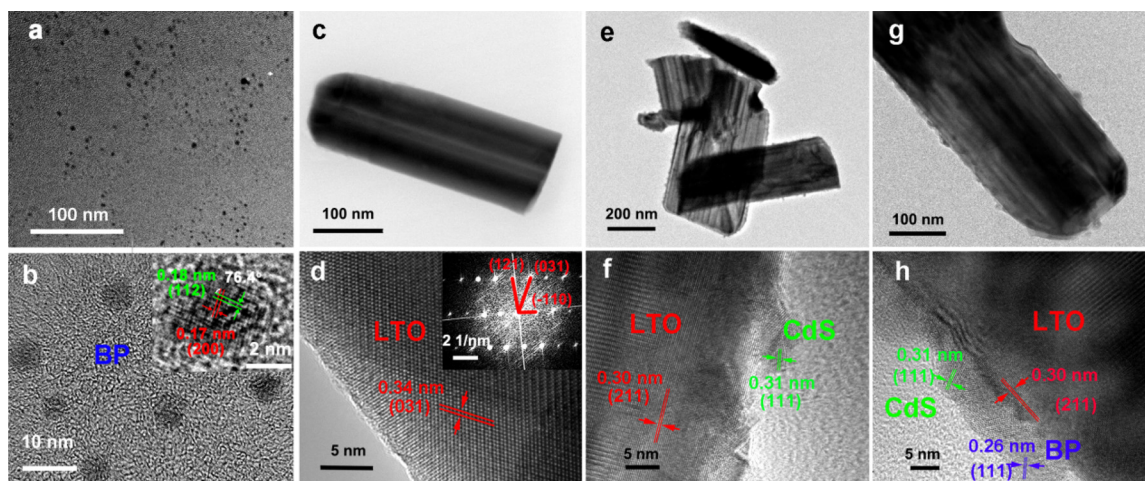


Fig. 2. TEM (a, c, e, and g) and HRTEM (b, d, f, and h) images of BP (a and b), LTO (c and d), CdS-LTO (e and f), and BP-CdS-LTO (g and h).

attributing to P–S bonds [29]. These results indicate the close combination among BP, CdS and LTO, including the strong interaction of CdS and LTO, as well as the connection of BP and CdS through P–S bonds.

To further confirm the bonding states of BP and CdS, we used DFT theoretical computation to identify the adsorption configuration of P at CdS surface. At the beginning, the P atoms were put in two different places of CdS surface to form P–Cd and P–S bond, as shown in Fig. 4a and c, respectively. The optimized results were obtained after a geometry relaxation process (Fig. 4b and d). The formation energy ( $E_f$ ) for these different structures is calculated to evaluate their structural stability, according to the following equation:  $E_f = E_{\text{tot}} - E_0[\text{CdS}] - E_p$ , where  $E_{\text{tot}}$  is the total energy for CdS with adsorbed P atoms,  $E_0[\text{CdS}]$  is the energy for CdS slab,  $E_p$  is the energy of one P atom referred to its bulk material [35]. According to the calculated results, when S atom of CdS bond with P atom (P–S), the  $E_f$  is -1.3 eV, while the  $E_f$  is -0.4 eV for P–Cd. One can conclude that the case of P–S bond is the most likely adsorption configuration of P at CdS surface [36].

Shown in Fig. S5a are the UV–vis–NIR diffuse reflectance spectra (DRS) of the samples. One can see that the bare LTO can absorb only UV light with wavelengths shorter than 380 nm. The derived electronic bandgap for LTO from the Tauc plots is 3.28 eV (Fig. S5b). CdS NPs

resulted from water bath approach exhibit visible light response with absorption edges at 511 nm, corresponding to 2.25 eV of bandgap energy. With a broad absorption from UV to NIR range, BP QDs have a narrow bandgap of 1.30 eV, which can be confirmed by the absorption spectra of BP QDs dispersed in NMP (Fig. S5c). When CdS is hybridized with LTO, the absorption threshold for LTO displays a slight red-shift. The main absorption of LTO is followed by a tail absorption which can be assigned to the absorption of CdS NPs. For BP-CdS-LTO, integrate absorptions of BP, CdS, and LTO are observed from UV to NIR range, showing its capability to utilize long-wavelength solar spectrum.

### 3.2. Photocatalytic $H_2$ production activity

The photocatalytic  $H_2$  production was evaluated over BP-CdS-LTO hybrid as a noble-metal free photocatalyst in the presence of  $\text{Na}_2\text{S}/\text{Na}_2\text{SO}_3$  as sacrificial agent. As shown in Fig. 5a, a trace amount of  $H_2$  was observed when bare LTO and BP were used as photocatalysts during simulated solar light irradiation, suggesting the fast recombination of photogenerated charges in pure LTO and BP. The evolved  $H_2$  amount over bare CdS was  $0.23 \text{ mmol g}^{-1}$  at the beginning of 30 min, while the subsequent increment of per half hour was 0.15,

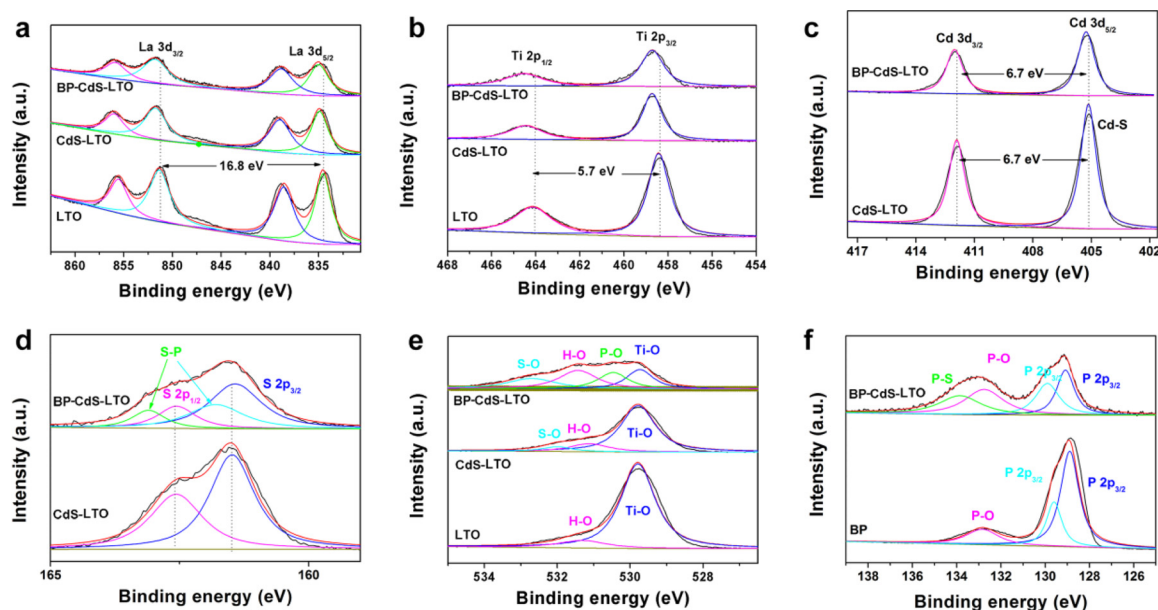
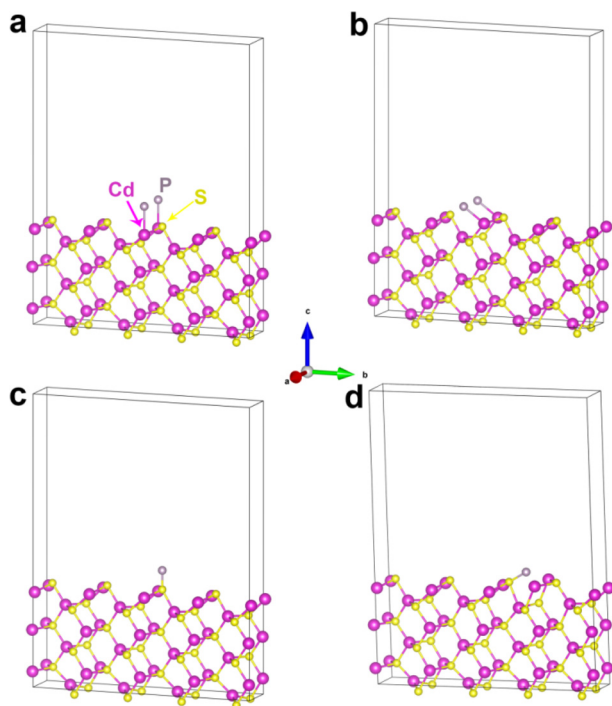


Fig. 3. High-resolution XPS of La 3d (a), Ti 2p (b), Cd 3d (c), S 2p (d), O 1s (e) and P 2p (f) in LTO, CdS-LTO, BP-CdS-LTO, and BP samples.



**Fig. 4.** Illustration of P coordinated with Cd (a and b) and S (c and d) sites of the CdS matrix before (a and c) and after (b and d) geometry optimization.

0.13, 0.06 and 0.04 mmol g<sup>-1</sup>. Due to the instability of CdS, the increase in hydrogen production decreased with time. In contrast, the amount of H<sub>2</sub> evolved from CdS-LTO increased with time, indicating that the formation of binary composite can not only decrease the electron-hole recombination within LTO but also enhance the stability of CdS. BP modification further improved the performance of CdS-LTO to generate 2.88 mmol g<sup>-1</sup> under UV-vis-NIR light for 3 h. However, without CdS NPs, merely 0.27 mmol g<sup>-1</sup> H<sub>2</sub> was detected under the similar condition using BP-LTO photocatalyst. These results indicate that the interaction between BP, CdS and LTO plays a crucial role in the photocatalytic H<sub>2</sub> production. A series of controlled trials demonstrated that the optimal amount of CdS NPs and BP QDs in BP-CdS-LTO was 3 and 1 wt%, respectively (Fig. S6), resulting in a H<sub>2</sub> production rate of

0.96 mmol g<sup>-1</sup> h<sup>-1</sup> in full solar spectrum region (Fig. 5b, black column). By putting a 420 or 700 nm long-pass filter between the reactor and light source, we tested the LTO, CdS-LTO and BP-CdS-LTO samples in generation of H<sub>2</sub> under vis-NIR or NIR light irradiation. As the irradiation wavelength was longer than 420 nm, the H<sub>2</sub> generation rate of BP-CdS-LTO (0.80 mmol g<sup>-1</sup> h<sup>-1</sup>) was 1.8 times those of CdS-LTO (0.44 mmol g<sup>-1</sup> h<sup>-1</sup>) (Fig. 5b, red column). As for NIR light ( $\lambda > 700$  nm) illumination, the photocatalytic H<sub>2</sub> production rate of BP-CdS-LTO was measured to be 0.26 mmol g<sup>-1</sup> h<sup>-1</sup> (Fig. 5b, blue column). Compared with analogous BP-based or noble metal-free photocatalysts, the high H<sub>2</sub> evolution rates in NIR region makes the BP-CdS-LTO composite an efficient photocatalyst for broad solar spectrum utilization (Table S1). As expected, LTO and CdS-LTO exhibited no obvious photocatalytic activity at wavelength longer than 400 and 700 nm, respectively, because the low energy photons coming from the filtered Xe lamp could not cause their bandgap photoexcitation.

In order to distinguish that the H<sub>2</sub> production activity of BP-CdS-LTO was driven by the light excitation of each component, the wavelength dependent AQE was measured. In Fig. 5c, the action spectrum of the AQE matched well with the absorption spectrum. Cyclic photocatalytic H<sub>2</sub> evolution experiments were performed to investigate the photocatalytic stability of BP-CdS-LTO. As shown in Fig. 5d, continuous H<sub>2</sub> evolution with long time irradiation indicates that BP-CdS-LTO can be used as a stable photocatalyst. The slight decrease of the activity during the recycling reactions might be induced by slight degradation of BP and/or loss of catalysts during centrifugation process. Furthermore, TEM image and Raman spectrum of BP-CdS-LTO after the photoreaction processes showed no obvious change in comparison with the initial ones (Fig. S7), suggesting that BP and CdS components of the ternary composite kept stable during photocatalytic evolution of H<sub>2</sub>.

### 3.3. Photoelectrochemical and electrochemical property

To enhance the photocatalytic performance, an efficient charge separation/transfer is crucial. For the sake of investigating the interfacial charge transport between BP, CdS and LTO under various light irradiation, current density potential (J-V) and EIS were studied when LTO, CdS-LTO, and BP-CdS-LTO film electrodes worked as photocathodes in a photoelectrochemical cell (PEC). Shown in Fig. S8a is the J-V curves of different electrodes without and with solar light irradiation. The photocurrent density of above photoelectrodes followed

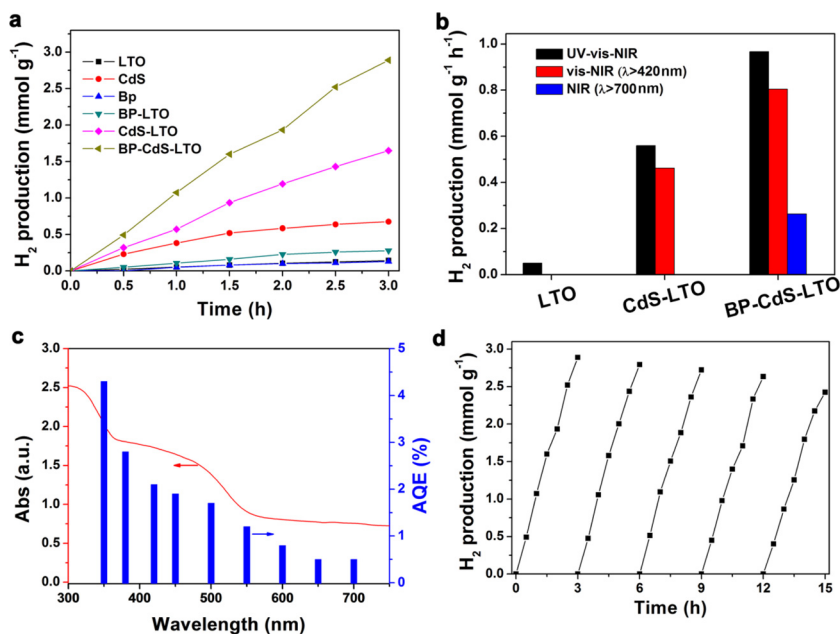


**Fig. 5.** Photocatalytic H<sub>2</sub> production over different samples under UV-vis-NIR irradiation (a). Comparison of H<sub>2</sub> production rate over different samples under UV-vis-NIR, vis-NIR and NIR light irradiation (b). DRS (left axis, red line) and AQE (right axis, blue column) of BP-CdS-LTO (c). Cycle stability test on BP-CdS-LTO photocatalytic H<sub>2</sub> production under UV-vis-NIR irradiation (d) (For interpretation of the references to colour in this figure legend, the reader is referred to the web version of this article).

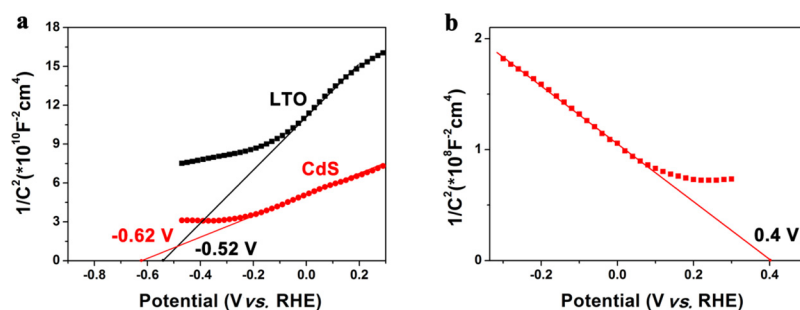


Fig. 6. Mott-Schottky plots of LTO and CdS (a), and BP (b).

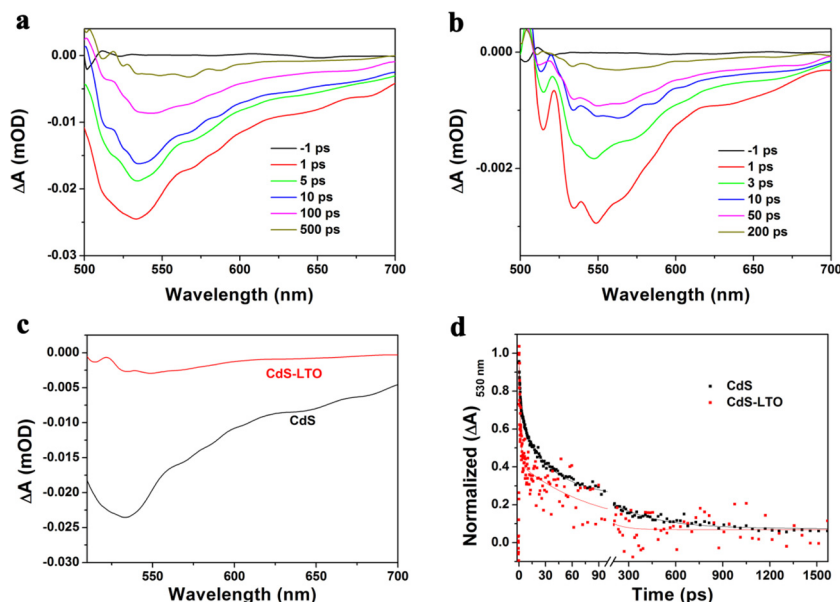


Fig. 7. Time-resolved transient absorption spectra of CdS (a), and CdS-LTO (b) measured with 460 nm excitation. Transient absorption spectra of CdS and CdS-LTO at early delay time (c). Normalized transient absorption traces observed at 530 nm (d), bold lines indicate multi-exponential curves fitted to kinetic traces.

Table 1

Lifetime ( $\tau_i$ ) and amplitudes ( $a_i$ ) of the transient absorption decays at the CdS signal region for different samples.

Sample	$a_1$	$\tau_1$ (ps)	$a_2$	$\tau_2$ (ps)	$a_3$	$\tau_3$ (ps)
CdS	0.31	$2.8 \pm 0.1$	0.36	$24 \pm 2$	0.33	$280 \pm 20$
CdS-LTO	0.57	$1.8 \pm 0.3$	0.43	$86 \pm 25$		

the same increasing trend as the hydrogen production rate (Fig. 5b), in which ternary BP-CdS-LTO material displayed the highest current density ( $-0.37 \text{ mA cm}^{-2}$  at  $-0.8 \text{ V}$  vs. Ag/AgCl electrode) when exposed to the light. The absorbed photons in the photoelectrodes are transferred to charges and the higher charge separation efficiency in BP-CdS-LTO results in higher photocurrent densities. EIS analysis was used to verify the electron mobility and internal resistance of BP-CdS-LTO electrode, by evaluating the diameter of semicircle arc. As shown in Fig. S8b, the diameters of the arc radius on the EIS Nyquist plot of BP-CdS-LTO electrode are smaller than those of LTO and CdS-LTO electrodes, indicating the improved electrical conductivity of the ternary composite [35]. Furthermore, different light sources (wavelengths longer than 420 and 700 nm and simulated solar light) were employed to examine the broad photoresponse properties of BP-CdS-LTO during J–V and EIS measurements. According to results in Fig. S8c and d, BP-CdS-LTO is demonstrated to be a promising broad-wavelength-range responsive material for the photoelectrochemical conversion of solar energy.

In addition, the band energy position of each component of BP-CdS-LTO ternary material was further determined. As shown in Fig. 6, the

intersection points, corresponding to the flat-band potential ( $V_{fb}$ ), in the Mott-Schottky plots are calculated to be  $-1.13$ ,  $-1.23$ , and  $-0.21 \text{ V}$  vs. Ag/AgCl electrode, i.e.,  $-0.52$ ,  $-0.62$ , and  $0.40 \text{ V}$  vs. RHE for LTO, CdS and BP, respectively [37]. The positive slope of Mott-Schottky curves in Fig. 6a indicate that both LTO and CdS are n-type semiconductors and their  $V_{fb}$  are approximately equal to the conduction band minimum (CBM) potential [38]. As for Mott-Schottky plot in Fig. 6b, the negative slope illuminates the p-type nature of BP and its  $V_{fb}$  corresponds to valence band maximum (VBM) potential. Therefore, taking the UV–vis–NIR absorption spectra results into consideration, CB and VB edge levels of LTO NSP, CdS NPs and BP QDs are about  $-0.52$  and  $2.76 \text{ V}$ ,  $-0.62$  and  $1.63 \text{ V}$ ,  $-0.90$  and  $0.40 \text{ V}$  vs. RHE, respectively.

### 3.4. Charge transfer dynamics

As a powerful analytical tool for understanding of fundamental photophysical processes, ultrafast transient absorption (TA) spectroscopy was carried out to study the effect of CdS and BP decoration on charge carrier dynamics over the BP-CdS-LTO system through directly observing the kinetics of electron transfer time-scale and carrier populations after the bandgap excitation. We firstly excited bare LTO using  $300 \text{ nm}$  pump light but no signal could be observed in the probe beam from  $430$  to  $750 \text{ nm}$ , probably because the TA signal of photo-induced holes of LTO is located in the UV range. Then, we successfully obtained the TA spectra of CdS NPs and CdS-LTO hybrids upon  $460 \text{ nm}$  pump light irradiation. Fig. 7 presents their typical differential absorption ( $\Delta A$ ) spectra, revealing a pronounced signal around  $530 \text{ nm}$  in



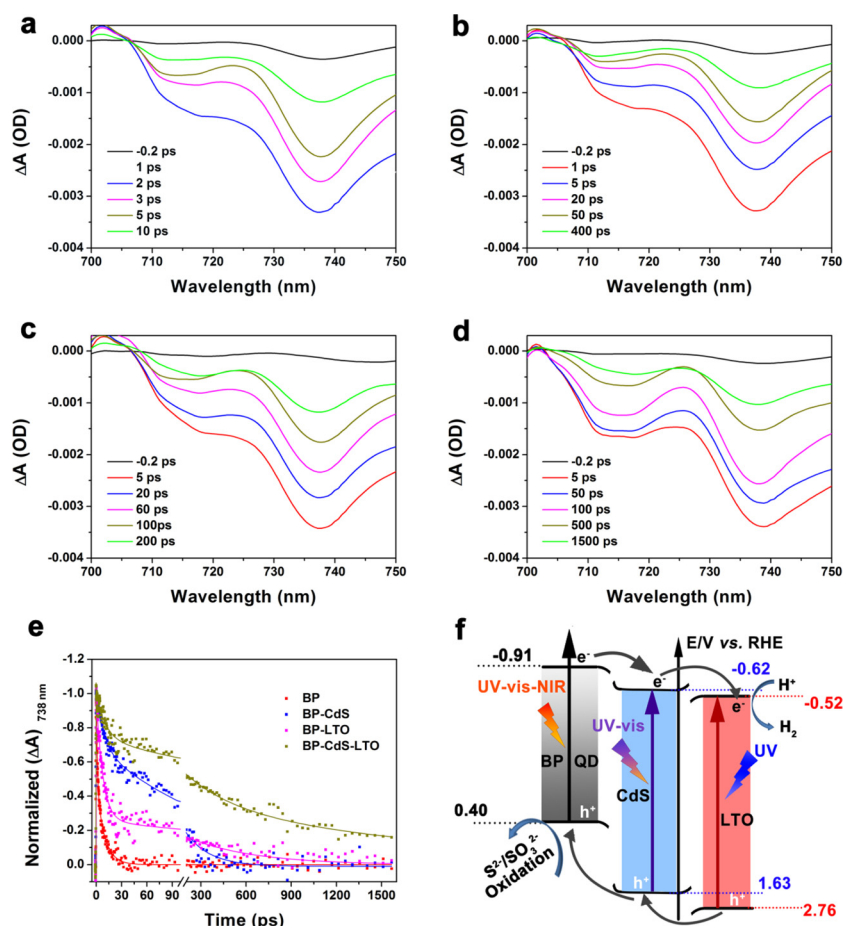


**Fig. 8.** Time-resolved transient absorption spectra of BP (a), BP-CdS (b), BP-LTO (c), and BP-CdS-LTO (d) measured with 620 nm excitation. Normalized transient absorption traces observed at 738 nm (e), bold lines indicate multi-exponential curves fitted to kinetic traces. Schematic illustration of electron transfer pathway in the BP-CdS-LTO system (f).

**Table 2**

Lifetime ( $\tau_i$ ) and amplitudes ( $a_i$ ) of the transient absorption decays at the BP signal region for different samples.

Sample	$a_1$	$\tau_1$ (ps)	$a_2$	$\tau_2$ (ps)	$a_3$	$\tau_3$ (ps)
BP	0.45	$1.5 \pm 0.5$	0.55	$11 \pm 2$		
BP-CdS	0.33	$8.0 \pm 4$	0.67	$160 \pm 70$		
BP-LTO	0.69	$7.0 \pm 4$	0.31	$440 \pm 110$		
BP-CdS-LTO	0.27	$10 \pm 3$	0.33	$320 \pm 80$	0.40	$1800 \pm 700$

the two samples (Fig. 7a and b) attributed to the stimulated radiation of CdS [22]. From the comparative  $\Delta A$  spectra at early delay time ( $\sim 2$  ps) in Fig. 7c, it was found that the intensity of stimulated radiation of CdS loaded on LTO was only one-tenth that of bare CdS, implying a rapid electrons transfer process from CdS to LTO [39]. At 10 ps after pulse laser excitation, the absorbance intensities at 530 nm of CdS-LTO showed 61.2% decrease, which are significantly enhanced compared with bare CdS (34.4%). This faster intensity decrease observed with CdS-LTO indicated the accelerated radiation decay kinetics. Fitting the time profiles of radiation recovery at 530 nm via a multi-exponential function, we evaluated the decay kinetics of the photogenerated electron-hole pairs in CdS components. The resulted transient absorption traces are displayed in Fig. 7d, and their corresponding lifetimes ( $\tau_i$ ) and amplitudes ( $a_i$ ) are summarized in Table 1 [40]. The radiation decay trace on the CdS was fitted to a three-exponential function with time constants of 2.8 ps (31%), 24 ps (36%), and 280 ps (33%), which were assigned to the recombination of electrons trapped at different defect states with the holes in CdS [41]. Differently, only two decay lifetimes were obtained for CdS-LTO: 1.8 ps (57%) and 86 ps (43%). The much shorter of radiation lifetime for CdS loaded on LTO demonstrated the existence of additional radiation deactivation path, i.e., charge

transfer process [42–44]. This extra route was extremely short (only 1.8 ps), and accounted for 57% of the overall electrons-holes recombination in CdS, attributing to the interfacial electron injection from CdS to LTO [44].

Following 620 nm pump light excitation, the time-resolved  $\Delta A$  spectra of samples BP, BP-CdS, BP-LTO, and BP-CdS-LTO are separately revealed in Fig. 8a–d. A broad bleach feature was observed in the range of 700–750 nm, being related to the holes photoexcited in BP [45]. In order to compare the bleach recovery dynamics of the different BP-mediated materials, Fig. 8e exhibits the normalized transient absorption decay at 738 nm. As summarized in Table 2, bare BP QDs showed two fast decay components, in which timescale of 1.5 ps corresponded to the exciton recovery to the ground state, and 10 ps could be ascribed to residual cooling of the trapped electrons in superficial defect states of BP [45]. The bleach recovery kinetics of BP components of BP-CdS, BP-LTO, and BP-CdS-LTO could be fitted to bi- or tri-exponential functions with two or three time constants, representing for different electron decay process in the composites. The shortest component with lifetime of only several picoseconds ( $\tau_1$ ) corresponded to the intrinsic recovery of BP, namely, the recombination of electron-hole pairs within BP. Second component,  $\tau_2$ , of several hundreds of picoseconds was due to the electrons injected from BP into the neighboring CdS or LTO within a short distance [24]. It took only 100–500 ps for the trapped electrons in CdS component of BP-CdS or LTO component of BP-LTO to recombine with the holes in BP component owing to the lack of effective diffusion. The second time constant ( $\tau_2$ ) of BP-CdS (160 ps) was far below that of BP-LTO (440 ps) and BP-CdS-LTO (320 ps), which may be attributed to the shorter electron diffusion distance in the 0D-0D (BP QDs-CdS NPs) system. The proportions of the transferred electrons (injection efficiency,  $1 - a_1$ ) in BP-CdS (67%) and BP-CdS-LTO (73%) systems were much larger than those in BP-LTO (31%) system, suggesting that the

formed S–P bonds between BP and CdS were conducive to the charge transfer from BP to CdS. The electron injection timescale in the BP–CdS system was also acquired as described in Fig. S9. The electron injection process from BP into CdS was ultrafast ( $\tau_{\text{inj}} = 4.0$  ps), while a rapid backflow process ( $\tau_{\text{re}} \approx 160$  ps) of electrons from CdS to BP was also observed subsequently [46]. For BP–CdS–LTO, there was a long lived component,  $\tau_3$ , which corresponds to the recombination of the long-distance diffused electrons from LTO via CdS and the holes in BP. The efficient charge carrier separation process in the BP–CdS–LTO was consequently demonstrated by such a long lifetime of 1800 ps.

The above results evidently demonstrate that electrons can transfer from BP QDs to LTO through CdS, and simultaneously CdS itself can release and inject electrons into LTO, endowing BP–CdS–LTO ternary composite with effective full solar spectrum activated photocatalytic activity. The possible mechanism for  $\text{H}_2$  evolution of BP–CdS–LTO is illustrated in Fig. 8f, basing on the band alignment of each component of this system. It is worth to be mentioned that, because of quantum confinement [47], the band gap of BP QDs (1.30 eV) is larger than that of bulk (ca. 0.30 eV) or flake-like BP (ca. 0.60 eV) [18,21]. Also, BP QDs possess an up-shifted edge position of the CB, which is higher than the CBM level of CdS and LTO. BP QD is stimulated to generate electrons and holes in CB and VB, respectively, during the irradiation of BP–CdS–LTO under UV, visible or NIR light. Based on thermodynamics principle, electrons in BP can deliver to CdS and LTO, while the formed S–P bonds establish a preferential pathway for charge transfer between BP and CdS. Meanwhile, CdS is also excited by UV–vis light. The above TA results clarified that those electrons from excited CdS unidirectionally transfer to the CB of LTO, where  $\text{H}^+$  (water) is reduced to  $\text{H}_2$ . Finally, holes are rapidly trapped by  $\text{S}^{2-}/\text{SO}_3^{2-}$  as a sacrificial electron donor.

#### 4. Conclusion

BP–CdS–LTO photocatalyst composed of wide-band gap semiconductor of LTO NSP and narrow-bandgap semiconductors of CdS NPs and BP QDs were synthesized for UV–vis–NIR light driven  $\text{H}_2$  production without any noble metal assistance. This ternary composite material exhibited the maximum  $\text{H}_2$  evolution rate of  $0.96 \text{ mmol g}^{-1} \text{ h}^{-1}$  in full solar spectrum region, significantly better than that of LTO, CdS, CdS–LTO and BP–LTO. The superior photocatalytic performance of BP–CdS–LTO was ascribed to the overall photoabsorption contribution, the dual role (electron relay and electron donor) of CdS NPs, as well as the appropriate band alignment and strong coupling between the three components. Femtosecond transient absorption spectroscopy gave a detail information of charge carrier transfer dynamics. It was demonstrated that the electrons could migrate from BP to CdS within several picoseconds, benefiting by the up-shifted CB edge of BP QDs and the formed S–P bonds between BP and CdS. Subsequently, an efficient charge separation was achieved through the rapid electrons delivery from CdS to LTO, prolonging the charge carrier lifetime of BP from ca. 10 ps to 1800 ps. Overall, the results indicated that the BP–CdS–LTO composite has great potential as a noble metal-free photocatalyst for wide range solar energy conversion.

#### Acknowledgment

This project is financially supported by National Natural Science Foundation of China (Grant Nos. 51472013, 51672106 and 21533010) and the National Key Research and Development Program of China (Grant 2017YFA0204800).

#### Appendix A. Supplementary data

Supplementary material related to this article can be found, in the online version, at doi:<https://doi.org/10.1016/j.apcatb.2018.10.007>.

#### References

- [1] S.J.A. Moniz, S.A. Shevlin, D.J. Martin, Z.-X. Guo, J. Tang, *Energy Environ. Sci.* 8 (2015) 731–759.
- [2] S. Chen, T. Takata, K. Domen, *Nat. Rev. Mater.* 2 (2017) 201750.
- [3] H. Park, H.-i. Kim, G.-h. Moon, W. Choi, *Energy Environ. Sci.* 9 (2016) 411–433.
- [4] Y.-J. Yuan, D. Chen, Z.-T. Yu, Z.-G. Zou, *J. Mater. Chem. A* 6 (2018) 11606–11630.
- [5] A. Fuentes, *Mater. Horiz.* 2 (2015) 453–461.
- [6] Y. Qu, X. Duan, *Chem. Soc. Rev.* 42 (2013) 2568–2580.
- [7] F. Meng, Z. Hong, J. Arndt, M. Li, M. Zhi, F. Yang, N. Wu, *Nano Res.* 5 (2012) 213–221.
- [8] F. Meng, J. Li, Z. Hong, M. Zhi, A. Sakla, C. Xiang, N. Wu, *Catal. Today* 199 (2013) 48–52.
- [9] J. Li, N. Wu, *Catal. Sci. Technol.* 5 (2015) 1360–1384.
- [10] B. Han, S. Liu, N. Zhang, Y.-J. Xu, Z.-R. Tang, *Appl. Catal. B-Environ.* 202 (2017) 298–304.
- [11] J. Chu, X. Han, Z. Yu, Y. Du, B. Song, P. Xu, *ACS Appl. Mater. Inter.* 10 (2018) 20404–20411.
- [12] X. Wang, F. Wang, Y. Sang, H. Liu, *Adv. Energy Mater.* 7 (2017) 1700473.
- [13] J. Tian, T. Yana, Z. Qiao, L. Wang, W. Li, J. You, B. Huang, *Appl. Catal. B-Environ.* 209 (2017) 566–578.
- [14] L. Li, Y. Yu, G.-J. Ye, Q. Ge, X. Ou, H. Wu, D. Feng, X.H. Chen, Y. Zhang, *Nat. Nanotechnol.* 9 (2014) 372–377.
- [15] H. Liu, Y. Du, Y. Deng, P.D. Ye, *Chem. Soc. Rev.* 44 (2015) 2732–2743.
- [16] A. Castellanos-Gomez, *J. Phys. Chem. Lett.* 6 (2015) 4280–4291.
- [17] J. Pang, A. Bachmatiuk, Y. Yin, B. Trzebicka, L. Zhao, L. Fu, R.G. Mendes, T. Gemming, Z. Liu, M.H. Rummeli, *Adv. Energy Mater.* 8 (2018) 1702093.
- [18] X. Zhu, T. Zhang, Z. Sun, H. Chen, J. Guan, X. Chen, H. Ji, P. Du, S. Yang, *Adv. Mater.* 29 (2017) 1605776.
- [19] H.U. Lee, S.C. Lee, J. Won, B.-C. Son, S. Choi, Y. Kim, S.Y. Park, H.-S. Kim, Y.-C. Lee, J. Lee, *Sci. Rep.* 5 (2015) 8691.
- [20] J. Li, S.K. Cushing, P. Zheng, T. Senty, F. Meng, A.D. Bristow, A. Manivannan, N. Wu, *J. Am. Chem. Soc.* 136 (2014) 8438–8449.
- [21] M. Zhu, X. Cai, M. Fujitsuka, J. Zhang, T. Majima, *Angew. Chem. Int. Edit.* 56 (2017) 2064–2068.
- [22] X. Cai, L. Mao, S. Yang, K. Han, J. Zhang, *ACS Energy Lett.* 3 (2018) 932–939.
- [23] X. Cai, L. Mao, J. Zhang, M. Zhu, M. Fujitsuka, T. Majima, *J. Mater. Chem. A* 5 (2017) 10442–10449.
- [24] X. Cai, M. Zhu, O.A. Elbanna, M. Fujitsuka, S. Kim, L. Mao, J. Zhang, T. Majima, *ACS Catal.* 8 (2018) 122–131.
- [25] G. Kresse, J. Furthmüller, *Phys. Rev. B* 54 (1996) 11169.
- [26] G. Kresse, D. Joubert, *Phys. Rev. B* 59 (1999) 1758.
- [27] X. Zhang, H. Xie, Z. Liu, C. Tan, Z. Luo, H. Li, J. Lin, L. Sun, W. Chen, Z. Xu, L. Xie, W. Huang, H. Zhang, *Angew. Chem. Int. Edit.* 54 (2015) 3653–3657.
- [28] F.Q. Zhou, J.C. Fan, Q.J. Xu, Y.L. Min, *Appl. Catal. B-Environ.* 201 (2017) 77–83.
- [29] C.D. Wagner, W.M. Riggs, L.E. Davis, J.F. Moulder, G.E. Muilenberg, *Handbook of X-Ray Photoelectron Spectroscopy*, Perkin-Elmer Corporation, Physical Electronics Division, USA, 1978.
- [30] Y. Yang, Y. Zhang, Z. Fang, L. Zhang, Z. Zheng, Z. Wang, W. Feng, S. Weng, S. Zhang, P. Liu, *ACS Appl. Mater. Interface* 9 (2017) 6950–6958.
- [31] S. Cao, X. Yan, Z. Kang, Q. Liang, Q. Liao, Y. Zhang, *Nano Energy* 24 (2016) 25–31.
- [32] J. Sun, Y. Sun, M. Pasta, G. Zhou, Y. Li, W. Liu, F. Xiong, Y. Cui, *Adv. Mater.* 28 (2016) 9797–+.
- [33] Z. Sun, H. Xie, S. Tang, X.-F. Yu, Z. Guo, J. Shao, H. Zhang, H. Huang, H. Wang, P.K. Chu, *Angew. Chem. Int. Edit.* 54 (2015) 11526–11530.
- [34] M. Zhu, C. Zhai, M. Fujitsuka, T. Majima, *Appl. Catal. B-Environ.* 221 (2018) 645–651.
- [35] L. Mao, X. Cai, H. Gao, X. Diao, J. Zhang, *Nano Energy* 39 (2017) 172–182.
- [36] Y. Zheng, Y. Jiao, Y. Zhu, Q. Cai, A. Vasileff, L.H. Li, Y. Han, Y. Chen, S.-Z. Qiao, *J. Am. Chem. Soc.* 139 (2017) 3336–3339.
- [37] X. Cai, J. Zhang, M. Fujitsuka, T. Majima, *Appl. Catal. B-Environ.* 202 (2017) 191–198.
- [38] J. Resasco, H. Zhang, N. Kornienko, N. Becknell, H. Lee, J. Guo, A.L. Brisenio, P. Yang, *ACS Central Sci.* 2 (2016) 80–88.
- [39] X.-L. Yin, G.-Y. He, B. Sun, W.-J. Jiang, D.-J. Xue, A.-D. Xia, L.-J. Wan, J.-S. Hu, *Nano Energy* 28 (2016) 319–329.
- [40] Z. Zhang, X. Jiang, B. Liu, L. Guo, N. Lu, L. Wang, J. Huang, K. Liu, B. Dong, *Adv. Mater.* 30 (2018) 1705221.
- [41] Y. Ben-Shahar, F. Scotognella, I. Kriegel, L. Moretti, G. Cerullo, E. Rabani, U. Banin, *Nat. Commun.* 7 (2016) 10413.
- [42] B. Yang, F. Zhang, J. Chen, S. Yang, X. Xia, T. Pullerits, W. Deng, K. Han, *Adv. Mater.* 29 (2017) 1703758.
- [43] B. Yang, J. Chen, F. Hong, X. Mao, K. Zheng, S. Yang, Y. Li, T. Pullerits, W. Deng, K. Han, *Angew. Chem. Int. Edit.* 56 (2017) 12471–12475.
- [44] J.E. Evans, K.W. Springer, J.Z. Zhang, *J. Chem. Phys.* 101 (1994) 6222–6225.
- [45] Y. Wang, G. Huang, H. Mu, S. Lin, J. Chen, S. Xiao, Q. Bao, J. He, *Appl. Phys. Lett.* 107 (2015) 93.
- [46] I. Grigioni, K.G. Stamplecoskie, D.H. Jara, M.V. Dozzi, A. Oriana, G. Cerullo, P.V. Kamat, E. Selli, *ACS Energy Lett.* 2 (2017) 1362–1367.
- [47] L. Liao, Q. Zhang, Z. Su, Z. Zhao, Y. Wang, Y. Li, X. Lu, D. Wei, G. Feng, Q. Yu, X. Cai, J. Zhao, Z. Ren, H. Fang, F. Robles-Hernandez, S. Baldelli, J. Bao, *Nat. Nanotechnol.* 9 (2014) 69–73.